

Quantifying the role of defects in monolayer graphene diffusion barriers

Patrick J. Strohbeen,¹ Vivek Saraswat,¹ Sebastian Manzo,¹ Michael S. Arnold,¹ and Jason K. Kawasaki^{1,*}

¹*Materials Science and Engineering, University of Wisconsin Madison, Madison, Wisconsin, 53706, USA*

(Dated: February 24, 2022)

We quantify the mechanisms for diffusion in Mn/graphene/semiconductor heterostructures, as a function of the defects induced by graphene sample preparation. These heterostructures are important for applications in spintronics; however, challenges in synthesizing graphene directly on technologically important substrates such as GaAs necessitate layer transfer steps, which can introduce defects into the graphene. *In-situ* photoemission spectroscopy measurements reveal that graphene grown directly on a Ge substrate reduces the diffusion coefficient by a factor of 1000 compared to samples without graphene ($D_{gr,direct} \sim 4 \times 10^{-18} \text{cm}^2/\text{s}$, $D_{no-gr} \sim 5 \times 10^{-15} \text{cm}^2/\text{s}$ at 500°C). Transferred graphene on Ge suppresses diffusion by a factor of 10 compared to no graphene ($D_{gr,transfer} \sim 4 \times 10^{-16} \text{cm}^2/\text{s}$). For both transferred and directly-grown graphene, the low activation energy ($E_a \sim 0.1 - 0.5 \text{ eV}$) suggests that Mn diffusion through graphene occurs primarily at graphene defects and the diffusivity prefactor D_0 scales with the defect density. Similar diffusion barrier performance is found on GaAs substrates; however, it is not currently possible to grow graphene directly on GaAs. Our results highlight the importance of developing graphene growth directly on functional substrates, to avoid the damage induced by layer transfer.

Graphene is a promising monolayer diffusion barrier for applications such as oxidation resistance [1], metal contacts to semiconductors [2, 3], and semiconductor spintronics [4]. Compared to conventional diffusion barriers that typically need to be tens of nanometers thick, graphene can remain effective as a diffusion barrier down to thicknesses of several atomic layers [2], and in select cases a single atomic layer [3]. This extreme thinness is highly attractive for applications where a nearly electronically transparent interface is desired, for example, spin injection via tunneling [4]. Moreover, recent reports of “remote epitaxy” suggest it is possible to synthesize epitaxial films through a monolayer graphene barrier [5–7], opening the possibility of epitaxial metal/graphene/semiconductor heterostructures that would otherwise not be stable due to significant metal/semiconductor interdiffusion [8].

A fundamental challenge, however, is that graphene cannot be synthesized directly on arbitrary substrates. While graphene can be grown by chemical vapor deposition (CVD) on Ge and noble metal surfaces (e.g., Cu, Ag, Pt), the high synthesis temperatures and catalytic reactions at the surface preclude growth directly on technologically important compound semiconductor substrates such as GaAs and InP. The use of non-native substrates requires post-synthesis graphene layer transfers, which can damage the graphene and create tears, wrinkles, and point defects. The impacts of this transfer process on effectiveness as a diffusion barrier have not been quantified, although the impacts of other intentional defects have been studied [9].

Here we quantify the effectiveness of layer-transferred vs directly-grown graphene as a monolayer diffusion barrier for Mn films, grown on GaAs and Ge substrates. The choice of Mn on a semiconductor is motivated by applications in spintronics. For example, the Mn-containing half

metallic ferromagnets NiMnSb and Co₂MnSi are promising materials for spin injection into GaAs [10, 11]. Sample structures consisted of a thin Mn film ($1.64 \times 10^{16} \text{ atoms/cm}^2$, $\sim 24 \text{ \AA}$) grown by molecular-beam epitaxy (MBE) on graphene-terminated Ge or GaAs (001) substrates. We evaluate two graphene preparations: (1) epitaxial graphene that is directly grown on a Ge substrate and (2) transferred graphene that is grown on a sacrificial Cu foil and then wet transferred to a Ge or GaAs substrate. *In-situ* x-ray photoemission spectroscopy (XPS) measurements reveal that both transferred and directly-grown graphene suppress diffusion into the semiconductor substrate. Directly-grown graphene on Ge significantly outperforms the layer transferred versions, decreasing the diffusivity at 500°C two orders of magnitude compared to the layer transferred version. We quantify the effective diffusivities and activation energies for Mn diffusion on graphene-terminated Ge and GaAs, and discuss mechanisms for diffusion.

RESULTS

Fig. 1 illustrates the differences between the directly-grown graphene versus graphene that has been layer transferred onto Ge. Direct growth of graphene on Ge (001) was performed by CVD at 910°C in an Ar/H₂ atmosphere using CH₄ as the precursor, as described in Ref. [12]. For the layer transferred graphene, the graphene was first grown by CVD on a Cu foil and then transferred to the Ge or GaAs substrate using a wet etch and transfer method (Methods). The directly-grown graphene/Ge and layer transferred graphene/Ge have similar Raman spectra, including a similar the D/G intensity ratio which is commonly used as a metric for graphene disorder (Fig. 1a). Clear differences, however, are observed in the scan-

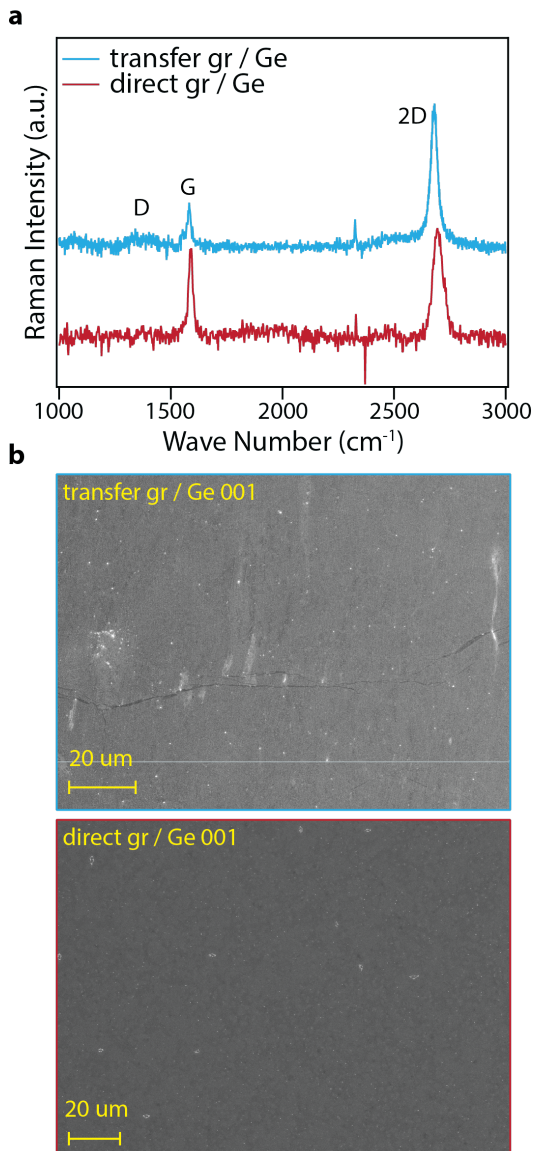


FIG. 1. **Defects in direct-growth vs layer transferred graphene.** (a) Raman spectra of the two different graphene (gr) preparations on Ge (001) surfaces. (b) Corresponding SEM images for the (top) layer transferred graphene and (bottom) directly-grown graphene on Ge (001) surfaces.

ning electron micrographs (Fig. 1b). Minimal extended defects are observed for direct-growth graphene (Figure 1b, bottom), whereas extended defects such as tears and wrinkles are observed for the layer transferred graphene on Ge (Figure 1b, top).

Figure 2c presents *in-situ* photoemission spectra tracking the evolution of Mn surface composition for Mn films grown on Ge substrates, with and without a graphene barrier. Each sample was subjected to a series of anneal steps at increasing temperature up to 500 °C. To eliminate variations in sample alignment, all spectra are normalized to the integrated Ge 3p core level intensity. For

the Mn film grown directly on Ge (black curves), with increasing anneal temperature the intensity of the Mn 2p rapidly decreases, corresponding to a decrease in the relative surface Mn composition. For Mn on transferred graphene (blue curves) and on direct-growth graphene (red curves), the Mn 2p core level decay is suppressed.

To compare the relative changes in surface Mn concentration, we fit the Mn 2p and Ge 3p core levels to Doniach-Sunjić [13] and Voigt lineshapes, respectively, and plot the relative change in Mn / Ge intensity ratio, $R_{Mn} = \frac{(I_{Mn2p}/I_{sub})_T}{(I_{Mn2p}/I_{sub})_0}$ (Fig. 2d, $sub = Ge\ 3p$). Here the numerator with subscript T refers to the Mn 2p / Ge 3p intensity ratio after anneal at temperature T and the denominator with subscript 0 refers to the Mn 2p / Ge 3p intensity ratio as-grown, before additional annealing. This normalization procedure cancels out the instrumental sensitivity, alignment, and photoemission cross section.

We find that the directly-grown graphene performs best as a diffusion barrier, with R_{Mn} decreasing to only 0.7 after an anneal up to 500°C, compared to $R_{Mn} = 0.05$ for the sample without graphene. Transferred graphene also suppresses interdiffusion compared to the bare substrate. For the no graphene sample there is a distinct onset of interdiffusion around 150°C, at which point R_{Mn} rapidly decreases. There is no distinct onset for the samples with graphene barriers. Together, these results demonstrate that both transferred and directly-grown graphene are effective solid state diffusion barriers for Mn in Ge, and that directly-grown graphene is most effective.

We next estimate the temperature-dependent diffusion length based on the relative changes in the Mn 2p / Ge 3p intensity ratio, R_{Mn} . For a very thin Mn film on a semi-infinite substrate, the solution to the diffusion equation is a half Gaussian composition profile (Fig. 2b)

$$c_{Mn}(z, \lambda) = \frac{n_{total}}{\sqrt{\pi}\lambda} \exp\left(\frac{-z^2}{4\lambda^2}\right) \quad (1)$$

where λ is the diffusion length and $n_{total} = 1.64 \times 10^{16}$ atoms/cm² is the total areal density of Mn deposited. We define the as-deposited initial condition such that the Mn concentration at the surface ($z = 0$) is equal to the density of pure Mn, i.e. $c_{Mn}(0, \lambda_0) = c_0 = 8.2 \times 10^{22}$ atoms/cm³. This yields an initial diffusion length of $\lambda_0 = 11$ Å. For simplicity, we let the Ge composition profile be $c_{Ge}(z) = c_0 - c_{Mn}(z)$, assuming that pure Mn, pure Ge, and the diffused Mn-Ge have approximately the same atomic densities and layer spacings.

From these composition profiles we calculate the expected intensity ratios for Mn 2p and Ge 3p, as a function of the diffusion length. The intensity of core level x is given by

$$I_x = f_x \sigma_x \sum_{i=0}^{\infty} n_{x,i} \exp\left(\frac{-z_i}{\lambda_{x,imfp} \cos\phi}\right) \quad (2)$$

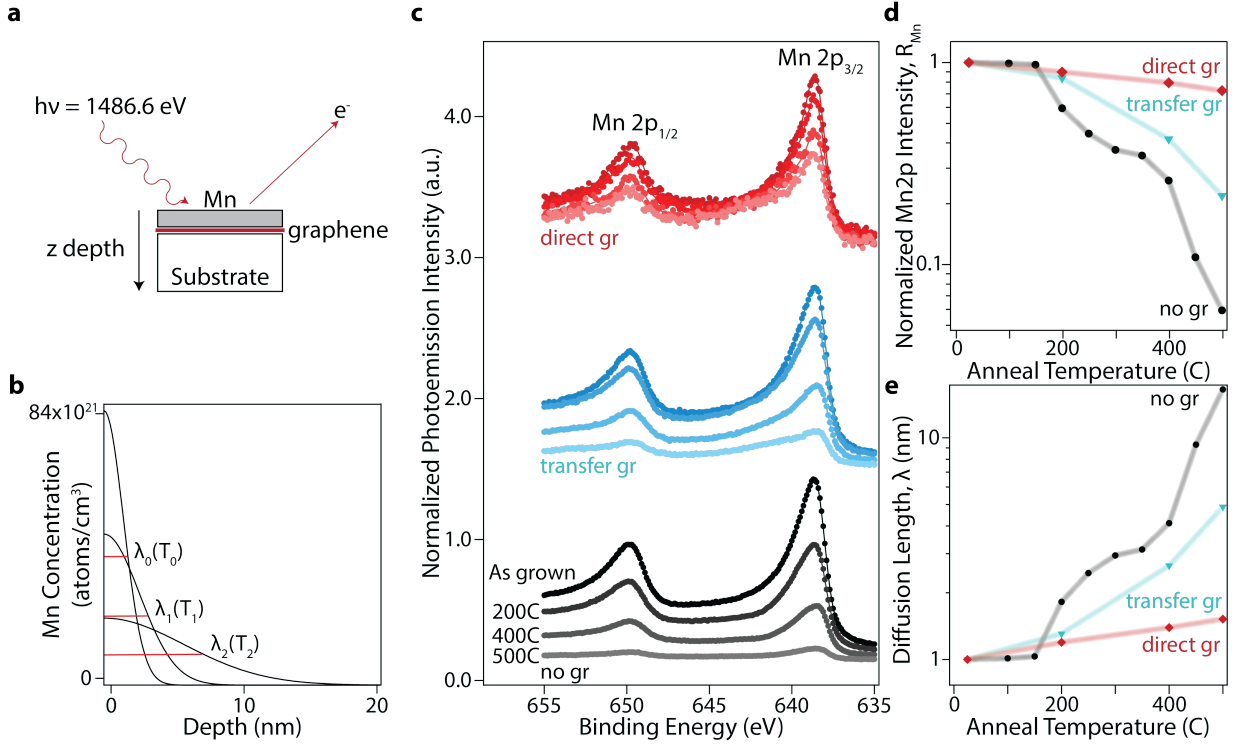


FIG. 2. **In-situ photoemission measurements of Mn on graphene(gr)/Ge.** (a) Schematic layer structure and measurement geometry. (b) Half Gaussian composition profiles as a function of depth from the surface. We use this model to extract diffusion length λ . (c) Mn 2p core level spectra for Mn thin films grown directly on bare Ge (black), transferred graphene/Ge (blue), and direct-growth graphene on Ge (red) at increasing anneal temperatures, using an Al $K\alpha$ source ($h\nu = 1486.6$ eV). Samples were rapidly heated to the anneal temperature, held for 5 minutes, rapidly cooled, and measured at room temperature. Symbols are experimental data and curves are fits to a Doniach-Sunjić lineshape. (d) Normalized Mn intensity ratio $R_{Mn} = \frac{(I_{Mn2p}/I_{sub})_T}{(I_{Mn2p}/I_{sub})_0}$, tracking the relative change in Mn surface composition as a function of anneal temperature T . For substrate normalization we use $sub = \text{Ge } 3p$. (e) Calculated Mn diffusion lengths λ at each anneal temperature.

where $n_{x,i}$ is the two-dimensional density of atomic layer i , z_i is the depth from the surface, $\lambda_{x,imfp}$ is the inelastic mean free path (20 Å for Mn 2p, 26 Å for Ge 3p, 22.1 Å for Ga 3p [14]), $\phi = 0^\circ$ is the emission angle from surface normal, f_x is an instrument sensitivity factor, and σ_x is the photoemission cross section. We rewrite the composition profiles in terms of atomic density, $n_{x,i} = d \cdot c_x(z, t)$, where d is the atomic layer spacing, and calculate the photoemission intensities I_{Mn} and I_{Ge} , subject to the initial condition $\lambda_0 = 11$ Å. We then compute the normalized Mn intensity ratio $R_{Mn} = \frac{(I_{Mn}/I_{Ge})_T}{(I_{Mn}/I_{Ge})_0}$, such that f_x and σ_x are cancelled out. In this way, the experimentally measured R_{Mn} is uniquely defined by the diffusion length λ after each sequential anneal.

Fig. 2(e) shows the estimated diffusion length, obtained by fitting the experimentally measured R_{Mn} to the calculated intensity ratios from Eqs 1 and 2. We find that compared to the bare Ge substrate, directly-grown graphene on Ge suppresses the diffusion length by a factor of just under 11 and layer transferred graphene suppresses the diffusion length by a factor 3.5, at a temperature of 500 °C.

In-situ photoemission measurements for Mn on GaAs substrates reveal similar behavior as the samples on Ge (Fig. 3). For the Mn directly on GaAs (Fig. 3a, black curves), in the as-grown spectrum we observe a secondary component at higher binding energy, indicative of reactions or secondary phases between Mn and GaAs. This reacted component grows with increased annealing. We attribute these secondary components to the formation of Mn_2As and MnGa phases, as has been observed previously at Mn/GaAs interfaces without graphene [15]. Comparison of the normalized Mn 2p intensity R_{Mn} and the estimated diffusion length reveal that like Ge, transferred graphene suppresses interdiffusion into GaAs.

We now use the diffusion length to estimate the diffusivity via $\lambda^2 = Dt$. Since each sample is subjected to a series of anneals at increasing temperature, we approximate the cumulative diffusion length squared after N anneal steps as a sum of the previous diffusion steps

$$\lambda_{total,N}^2 = \sum_{i=1}^N D(T_i) \Delta t_i, \quad (3)$$

where Δt_i is the time increment of anneal step i and

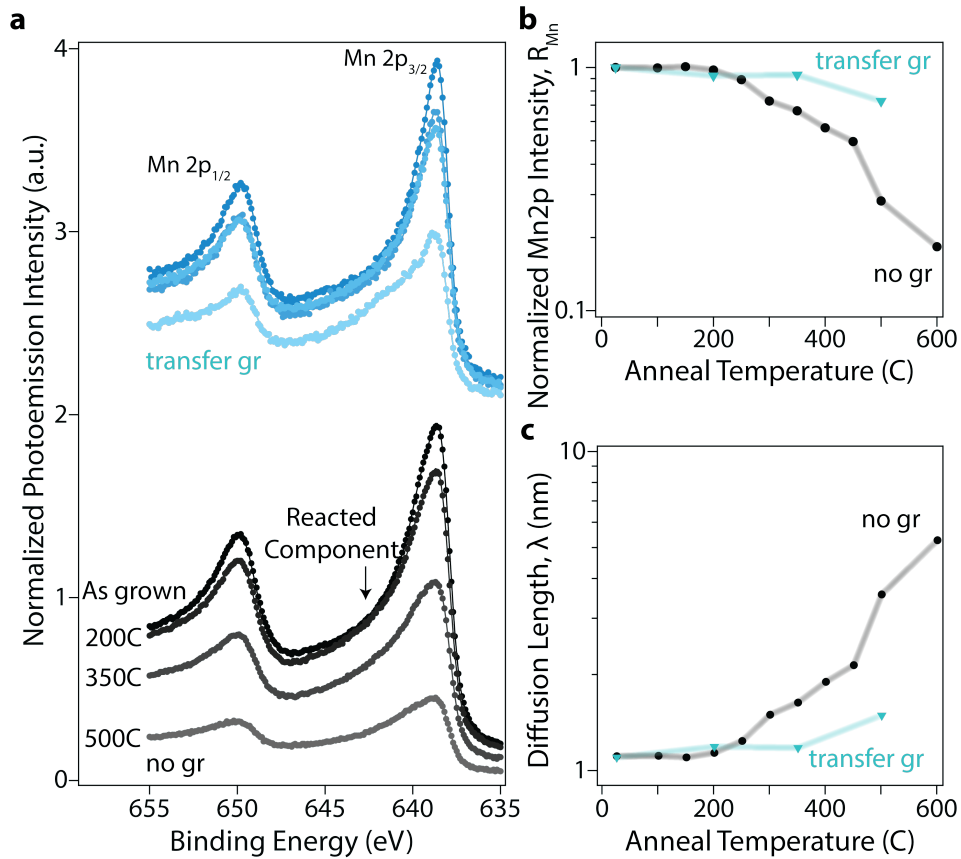


FIG. 3. **In-situ photoemission measurements of Mn on graphene(gr)/GaAs.** (a) Core level spectra and fits for Mn/GaAs (black) and Mn/transferred-gr/GaAs (blue) at increasing anneal temperatures. Data points represent experimental photoemission results and the traces represent the fits. (b) Normalized Mn intensity $R_{Mn} = \frac{(I_{Mn2p}/I_{sub})T}{(I_{Mn2p}/I_{sub})_0}$, tracking the relative change in Mn surface composition as a function of anneal temperature T . For substrate normalization we use $sub = \text{Ga } 3p$. (c) Calculated diffusion lengths at each anneal temperature.

$D(T_i)$ is the diffusivity from the anneal at temperature T_i . Since each anneal is for a constant amount of time ($\Delta t_i = 5$ minutes), we rewrite Equation 3 to solve for $D(T_i)$ contribution of an individual anneal step.

$$D(T_{i=N}) = \frac{\lambda_{total,N}^2}{\Delta t} - \sum_{m=1}^{N-1} D(T_m) \quad (4)$$

We plot the diffusivity $D(T_i)$ as a function of temperature in Fig. 4. From an Arrhenius fit, $D(T) = D_0 \exp(-E_a/k_B T)$, we extract activation energies E_a and diffusivity prefactors D_0 as listed in Table I. We find that at 500 °C, the diffusivity for Mn on directly-grown graphene / Ge (red curve) is a factor of 1000 lower than the diffusivity on bare Ge (black curve). Mn on transferred graphene / Ge is only a factor of 10 lower (blue curve). Similar behavior is observed for transferred graphene/GaAs compared to bare GaAs. To benchmark the accuracy of our method, we find that our experimentally determined diffusivities for Mn on bare GaAs (Fig. 4(b), filled black circles) are in good agreement with previous experiments (open black circles) [16–18].

| | D_0 (cm ² /s) | E_a (eV) | $D(500^\circ\text{C})$ (cm ² /s) |
|---------------------|----------------------------|------------|---|
| Ge | 6.0×10^{-10} | 0.81 | 5×10^{-15} |
| transfer gr/Ge | 6.0×10^{-13} | 0.50 | 4×10^{-16} |
| direct-growth gr/Ge | 3.0×10^{-17} | 0.13 | 4×10^{-18} |
| GaAs | 1.3×10^{-11} | 0.79 | 4×10^{-16} |
| transfer gr/GaAs | 5.2×10^{-17} | 0.21 | 7×10^{-18} |

TABLE I. Prefactors D_0 , activation energies E_a , and diffusivity at 500 °C for Mn diffusion into Ge and GaAs, extracted from in-situ XPS. We compare Mn grown directly on bare Ge or GaAs, with samples that contain a transferred or directly-grown graphene (gr) diffusion barrier.

DISCUSSION

We now discuss the mechanisms for diffusion based on the experimentally determined E_a and D_0 . Our experimentally determined activation energy of 0.8 eV for Mn diffusing into bare GaAs and Ge agrees well with previous experiments and DFT calculations for Mn interstitial diffusion into GaAs (0.7–0.8 eV [19]). Substitutional diffusion is expected to exhibit a higher activation energy

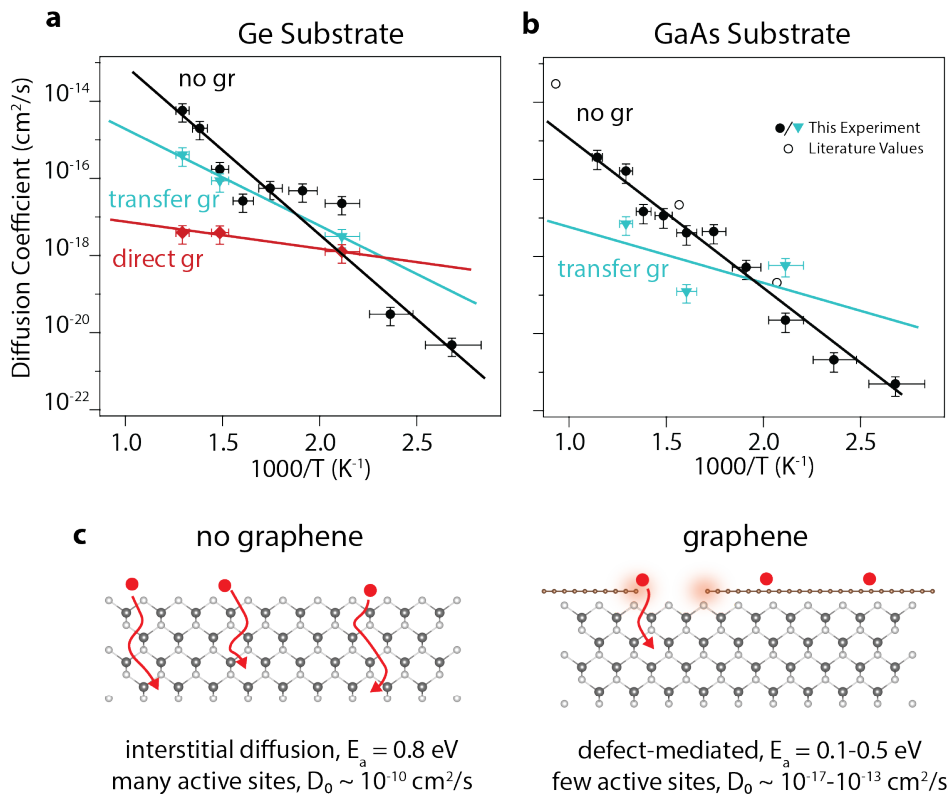


FIG. 4. **Calculated diffusion coefficients for Mn on Ge and GaAs, with and without graphene (gr).** (a) Diffusivity vs inverse temperature for Mn/Ge (black), Mn/layer transferred graphene/Ge (blue), and Mn/direct-growth graphene/Ge (red). Symbols are experimental data, the line is an Arrhenius fit. (b) Diffusivity vs inverse temperature for Mn/GaAs (black) and Mn/layer transferred graphene/GaAs (blue). The open symbols represent previously reported diffusivity for Mn on GaAs (no graphene) from Refs. [16–18]. (c) Schematic diffusion processes.

of 2-3 eV [20].

In comparison, E_a for Mn on graphene-terminated substrates is considerably lower: 0.1 eV for directly-grown graphene on Ge, and 0.2-0.5 eV for transferred graphene on GaAs and Ge. We speculate that the activation energies are lower on graphene-terminated substrates than on bare substrates due to reactions catalyzed at graphene defects, since graphene defects are known to be chemically active [2, 21]. In contrast, diffusion through pristine graphene is expected to have a very large activation energy barrier of $E_a \sim 12$ eV [22], since the effective pore size of graphene is small (~ 0.7 Å radius of a carbon ring, less than half the radius of a Mn atom). Therefore, we expect that Mn diffusion through graphene occurs primarily through defects.

While a low activation energy barrier favors a large diffusivity, the origin of the dramatic decrease of diffusivity for graphene-terminated samples is the reduction of the prefactor D_0 . We interpret D_0 to scale as an attempt rate for diffusion. For Mn on bare GaAs and Ge substrates, the attempt rates of $10^{-11} - 10^{-10}$ cm²/s are high because there are many available sites for interstitial diffusion into the substrate. On the other hand, at-

tempt rates are lower on the graphene-terminated substrates because Mn diffusion through graphene requires a defect in the graphene. This rate is higher for layer transferred graphene ($10^{-17} - 10^{-13}$ cm²/s) than for directly-grown graphene (10^{-17} cm²/s), since the layer-transferred graphene has a higher defect density.

CONCLUSIONS

Our results show that layer-transferred and directly-grown graphene suppress Mn diffusion into semiconductor substrates. The directly-grown graphene displays superior diffusion barrier performance due to a lower defect density. In our samples the Raman D/G intensity ratio is not a good predictor of graphene’s performance as a diffusion barrier. Translating these performance enhancements to functional substrates at wafer scale will require direct graphene synthesis approaches on the substrate of interest. For example, CVD approaches using small molecules [23], activated precursors [24], or plasma-enhanced CVD processes [25–27] show promise for reducing the graphene synthesis temperature, and may be a route for graphene growth directly on GaAs and other

technologically important compound semiconductors.

METHODS

CVD growth of graphene on Ge (001) and Cu foils. We use two preparations of graphene: graphene that is grown by chemical vapor deposition (CVD) directly on Ge (001), and graphene that is grown by CVD on Cu foils and then layer transferred onto Ge (001) or GaAs (001). For CVD graphene growth on Ge (001) we followed growth conditions described in Refs. [12, 28]. CVD graphene on Cu foils was performed at 1050 °C using ultra high purity CH₄, as described in Ref. [7].

Graphene transfer onto Ge (001) and GaAs (001). Our graphene transfer process is similar to other polymer-assisted wet transfers reported in previous works [7, 29]. The graphene/Cu foils were cut into 5 by 5 mm pieces and flattened using cleaned glass slides. Approximately 300 nm of 495K C2 PMMA (Chlorobenzene base solvent, 2% by wt., MicroChem) was spin coated on the graphene/Cu foil substrate at 2000 RPM for 2 minutes and left to cure at room temperature for 24 hours. Graphene on the backside of the Cu foil was removed via reactive ion etching using 90 W O₂ plasma at a pressure of 100 mTorr for 30s. The Cu foil was then etched by placing the PMMA/graphene/Cu foil stack on the surface of an etch solution containing 1-part ammonium persulfate (APS-100, Transene) and 3-parts H₂O. After 16 hours of etching at room temperature, the floating PMMA/graphene membrane was scooped up with a clean glass slide and sequentially transferred into five 5-minute water baths to rinse the etch residuals. Prior to scooping the graphene with the GaAs (001) substrate, the native oxide is etched in a 10% HCl bath for 30 seconds. The GaAs is then rinsed in isopropanol and nitrogen dried. Prior to scooping with the Ge (001) substrate, the native oxide is etched in a hot (90°C) RO water bath for 15 minutes. Immediately after the etching process, the substrate is used to scoop the PMMA/graphene membrane from the final water bath. To remove water at the graphene/substrate interface, samples were baked in air at 50C for 5 minutes, then slowly ramped to 150°C and baked for another 10 minutes. The PMMA was dissolved by submerging the sample in an acetone bath at 80C for 3 hours. Samples are then rinsed in isopropanol and dried with nitrogen.

Manganese film growth. Bare Ge substrates were sequentially degreased for 15 minutes in acetone, 15 minutes in isopropanol baths, and then etched in reverse-osmosis (RO) water at 90°C for 30 minutes. No solvent treatments were performed to the bare GaAs substrates. All samples were indium-bonded to a molybdenum sample holder to ensure good thermal contact. Samples were outgassed in a high vacuum load lock ($p < 5 \times 10^{-8}$) for at least 1 hour at 150°C prior to transferring into

the ultra-high vacuum (UHV) molecular beam epitaxy (MBE) chamber ($P < 5 \times 10^{-10}$).

In the MBE chamber, the graphene-terminated samples were further outgassed at $\sim 300^\circ\text{C}$ to remove residual organic contaminants, and then annealed at 760°C (Ge) or 595°C (GaAs) to remove surface oxides. Removal of surface oxides was confirmed via reflection high energy electron diffraction (RHEED). For the bare GaAs substrate, a thick GaAs buffer layer was grown to smoothen the surface before Mn growth. No buffer layers were grown on the other samples.

Thin Mn films (1.64×10^{16} atoms/cm²) were grown at room temperature, using an elemental effusion cell. The thickness was measured using an *in-situ* quartz crystal microbalance (QCM) that has been calibrated through *ex-situ* Rutherford backscattering spectroscopy (RBS).

In-situ photoemission. Immediately following growth, samples were transferred through an ultrahigh vacuum manifold ($p < 5 \times 10^{-9}$ Torr) to a connected photoemission spectroscopy chamber. X-ray photoemission spectroscopy (XPS) measurements were conducted using a non-monochromated Omicron DAR-400 dual anode x-ray source (Al K_α: 1486.6 eV) and an Omicron EA125 hemispherical analyzer. The total energy resolution of the analyzer in the experimental configuration was measured to be 1.08eV using an Au standard. The photoemission chamber pressure was maintained at $< 3 \times 10^{-10}$ Torr during the measurements.

At each anneal step the samples were ramped from room temperature to the desired anneal setpoint temperature over 5 minutes. The sample was held at temperature ($\pm 10^\circ\text{C}$) for 5 minutes and then rapidly cooled to room temperature. Sample temperature was measured by a thermocouple attached to the sample manipulator, roughly 1 cm away from the sample. The thermocouple was calibrated using the melting point of indium and the arsenic desorption temperature of As-capped GaAs. The sample was transferred immediately following the cool down back into the photoemission stage before beginning the next XPS measurement.

Raman and scanning electron microscopy. Graphene was characterized using field emission scanning electron microscopy (SEM) (Zeiss LEO 1530 Gemini). Raman spectroscopy was performed using a 532 nm wavelength laser (Thermo Scientific DXR Raman Microscope). The laser power is kept below 5 mW in order to prevent damage to the graphene.

ACKNOWLEDGMENT

Mn film growth and photoemission studies were supported by the National Science Foundation (DMR-1752797). Graphene synthesis and characterization are supported by the U.S. Department of Energy, Office of Science, Basic Energy Sciences, under award no. DE-

SC0016007. We gratefully acknowledge the use of Raman and electron microscopy facilities supported by the NSF through the University of Wisconsin Materials Research Science and Engineering Center under Grant No. DMR-1720415.

* jkawasaki@wisc.edu

- [1] M. Topsakal, H. Şahin, and S. Ciraci, *Physical Review B* **85**, 155445 (2012).
- [2] S. S. Roy and M. S. Arnold, *Advanced Functional Materials* **23**, 3638 (2013).
- [3] J. Hong, S. Lee, S. Lee, H. Han, C. Mahata, H.-W. Yeon, B. Koo, S.-I. Kim, T. Nam, K. Byun, et al., *Nanoscale* **6**, 7503 (2014).
- [4] E. Cobas, A. L. Friedman, O. M. van't Erve, J. T. Robinson, and B. T. Jonker, *Nano letters* **12**, 3000 (2012).
- [5] Z. Lu, X. Sun, W. Xie, A. Littlejohn, G.-C. Wang, S. Zhang, M. A. Washington, and T.-M. Lu, *Nanotechnology* **29**, 445702 (2018).
- [6] Y. Kim, S. S. Cruz, K. Lee, B. O. Alawode, C. Choi, Y. Song, J. M. Johnson, C. Heidelberger, W. Kong, S. Choi, et al., *Nature* **544**, 340 (2017).
- [7] D. Du, S. Manzo, C. Zhang, V. Saraswat, K. T. Genser, K. M. Rabe, P. M. Voyles, M. S. Arnold, and J. K. Kawasaki, *Nature communications* **12**, 1 (2021).
- [8] T. Sands, C. Palmstrøm, J. Harbison, V. Keramidias, N. Tabatabaie, T. Cheeks, R. Ramesh, and Y. Silberberg, *Materials Science Reports* **5**, 99 (1990).
- [9] S. Oh, Y. Jung, and J. Kim, *Journal of Vacuum Science & Technology A: Vacuum, Surfaces, and Films* **33**, 061510 (2015).
- [10] R. Farshchi and M. Ramsteiner, *Journal of Applied Physics* **113**, 7.1 (2013).
- [11] X. Dong, C. Adelman, J. Xie, C. Palmstrøm, X. Lou, J. Strand, P. Crowell, J.-P. Barnes, and A. Petford-Long, *Applied Physics Letters* **86**, 102107 (2005).
- [12] B. Kiraly, R. M. Jacobberger, A. J. Mannix, G. P. Campbell, M. J. Bedzyk, M. S. Arnold, M. C. Hersam, and N. P. Guisinger, *Nano Lett.* **15**, 7414 (2015).
- [13] S. Doniach and M. Sunjic, *J. Phys. C: Solid State Phys.* **3** (1970).
- [14] C. J. Powell and A. Jablonski, National Institute of Standards and Technology (2010).
- [15] J. L. Hilton, B. D. Schultz, S. McKernan, and C. J. Palmstrøm, *Appl. Phys. Lett.* **84** (2004).
- [16] M. S. Seltzer, *J. Phys. Chem. Solids* **26** (1965).
- [17] J. Adell, I. Ulfat, L. Ilver, J. Sadowski, K. Karlsson, and J. Kanski, *J. Phys.: Condens. Matter* **23** (2011).
- [18] O. V. Vikhrova, Y. A. Danilov, M. N. Drozdov, B. N. Zvonkov, and I. L. Kalent'eva, *J. Synch. Investig.* **6** (2012).
- [19] K. W. Edmonds, P. Boguslawski, K. Y. Wang, R. P. Champion, S. N. Novikov, N. R. S. Farley, B. L. Gallagher, C. T. Foxon, M. Sawicki, T. Dietl, et al., *Phys. Rev. Lett.* **92** (2004).
- [20] H. Raebiger, M. Ganchenkova, and J. von Boehm, *Appl. Phys. Lett.* **89** (2006).
- [21] T. Yoon, J. H. Mun, B. J. Cho, and T.-S. Kim, *Nanoscale* **6** (2014).
- [22] O. Leenaerts, B. Parteons, and F. M. Peeters, *Appl. Phys. Lett.* **93** (2008).
- [23] Z. Li, P. Wu, C. Wang, X. Fan, W. Zhang, X. Zhai, C. Zeng, Z. Li, J. Yang, and J. Hou, *ACS nano* **5**, 3385 (2011).
- [24] S. Lee, M. F. Toney, W. Ko, J. C. Randel, H. J. Jung, K. Munakata, J. Lu, T. H. Geballe, M. R. Beasley, R. Sinclair, et al., *ACS nano* **4**, 7524 (2010).
- [25] R. Vishwakarma, R. Zhu, A. A. Abuelwafa, Y. Mabuchi, S. Adhikari, S. Ichimura, T. Soga, and M. Umeno, *ACS Omega* **4**, 11263 (2019).
- [26] J. Mischke, J. Pennings, E. Weisenseel, P. Kerger, M. Rohwerder, W. Mertin, and G. Bacher, *2D Mater.* **7** (2020).
- [27] N. Li, Z. Zhen, R. Zhang, Z. Xu, Z. Zheng, and L. He, *Sci. Rep.* **11** (2021).
- [28] G. Wang, M. Zhang, Y. Zhu, G. Ding, D. Jiang, G. Qinglei, S. Liu, X. Xie, P. K. Chu, Z. Di, et al., *Sci. Rep.* **3** (2013).
- [29] H. Park, C. Lim, C.-J. Lee, J. Kang, J. Kim, M. Choi, and H. Park, *Nanotechnology* **29** (2018).